Ground-state phase diagram of the three-band Hubbard model from density matrix embedding theory

Zhi-Hao Cui,[1] Chong Sun,[1] Ushnish Ray,[1] Bo-Xiao Zheng,[2,1,3] Qiming Sun,[2,1] and Garnet Kin-Lic Chan[1,*]

[1]*Division of Chemistry and Chemical Engineering, California Institute of Technology, Pasadena, California 91125, United States*
[2]*AxiomQuant Investment Management LLC, Shanghai 200120, China*
[3]*Department of Chemistry, Princeton University, Princeton, New Jersey 08544, United States*

(Dated: October 30, 2021)

We determine the ground-state phase diagram of the three-band Hubbard model across a range of model parameters using density matrix embedding theory. We study the atomic-scale nature of the antiferromagnetic (AFM) and superconducting (SC) orders, explicitly including the oxygen degrees of freedom. All parametrizations of the model display AFM and SC phases, but the decay of AFM order with doping is too slow compared to the experimental phase diagram, and further, coexistence of AFM and SC orders occurs in all parameter sets. The local magnetic moment localizes entirely at the copper sites. The magnetic phase diagram is particularly sensitive to Δ_{pd} and t_{pp}, and existing estimates of the charge transfer gap Δ_{pd} appear too large in so-called minimal model parametrizations. The electron-doped side of the phase diagram is qualitatively distinct from the hole-doped side and we find an unusual two-peak structure in the SC in the full model parametrization. Examining the SC order at the atomic scale, within the larger scale $d_{x^2-y^2}$-wave SC pairing order between Cu-Cu and O-O, we also observe a local $p_{x(y)}$ [or $d_{xz(yz)}$]-symmetry modulation of the pair density on the Cu-O bonds. Our work highlights some of the features that arise in a three-band versus one-band picture, the role of the oxygen degrees of freedom in new kinds of atomic-scale SC orders, and the necessity of re-evaluating current parametrizations of the three-band Hubbard model.

I. INTRODUCTION

The three-band Hubbard model, also known as the Emery model [1], is generally believed to contain the essential physics of the high-T_c cuprates that arises from the interplay between the copper $d_{x^2-y^2}$ and oxygen $p_{x(y)}$ orbitals in the CuO_2 layers. Given the complexity of the model, commonly, the three-band model is further simplified and several simpler low-energy Hamiltonians have been proposed, such as the one-band Hubbard model [2, 3], t-J model [3, 4], and two-band model [5]. The first two are effective one-band models and are equivalent in the strong-coupling limit. In particular, the two-dimensional (2D) one-band Hubbard model has been extensively investigated using various numerical approaches (see Refs. [6, 7] and the references therein). Much of the physics seen in high-T_c materials, e.g. d-wave pairing, density waves, the pseudogap phase and stripe order, has been observed in studies of the simpler one-band Hubbard model within certain ranges of parameters [7].

However, despite the progress in understanding the one-band Hubbard model and its variants, there are still important reasons to go beyond the one-band picture to study the original three-band model directly. For instance, (a) some important physics may be lost in the reduction to the one-band approximation (such as a role for the oxygen degrees of freedom in the pseudogap phase [8]), (b) near degeneracies of competing states seen in the one-band case [7] may in fact be resolved with the additional degrees of freedom of the three-band model, and (c) the three-band model retains the atomic structure of the CuO_2 layer and thus has a direct link to the structure of real materials as well as experimental measurements of orders at the atomic scale. Previously, the three-band Hubbard model has been investigated with several numerical methods, including direct simulations of finite lattices [by exact diagonalization (ED) [9–15], quantum Monte Carlo (QMC) [15–23], density matrix renormalization group (DMRG) [22, 24–26], and the random phase approximation [27–29]] and via Green's function based embedding theories [such as dynamical mean-field theory (DMFT) and its cluster extensions [30–35], and the variational cluster approximation (VCA) [36, 37]]. However, due to the complexity of the model, unlike in the one-band case, a consensus on much of the physics has yet to be reached.

Over the past few years, density matrix embedding theory (DMET) [38] has emerged as a powerful cluster embedding method. The basic idea of DMET is similar to that of (cellular) DMFT in the sense that they both map an infinite lattice to an impurity model with an environment that can be described by bath degrees of freedom, and the impurity model is self-consistently improved by matching physical quantities between a single-particle lattice solution and the correlated cluster (impurity) calculation. Technically, however, DMET has a different structure to Green's function based embedding methods, and is formulated without frequency dependence and with a finite set of bath orbitals (bounded by the number of impurity orbitals). The lack of frequency-dependent quantities means that DMET calculations can utilize efficient ground-state impurity solvers that can typically treat larger clusters than can be addressed by solvers that target the impurity Green's function. DMET has been applied to a wide range of fermionic lattice models [7, 38–42], *ab initio* chemical Hamiltonians [43–48], and nonfermionic systems [49, 50], as well as excited states [51, 52] and time-dependent problems [53]. For a detailed review of DMET, we refer to Ref. [44].

In earlier work, DMET successfully provided an accurate description of the ground-state orders of the one-band Hubbard

* gkc1000@gmail.com

model [40], including in the difficult underdoped region [7]. In this work, we therefore attempt to understand the more complicated three-band Hubbard model using DMET. As we shall see, we can use DMET to provide a detailed description of the ground-state phases and orders as a function of doping, including the doping asymmetry and atomic-scale orders that are new to the three-band case. Another complication of the three-band model is the much larger parameter space than the one-band case. We use both existing parametrizations that have been published in the literature, as well as explicitly model the influence of different individual parameters on the orders. Our findings provide insights into the detailed picture of magnetic and superconducting orders that is provided by three-band models.

II. MODELS AND METHODS

A. Model parametrization

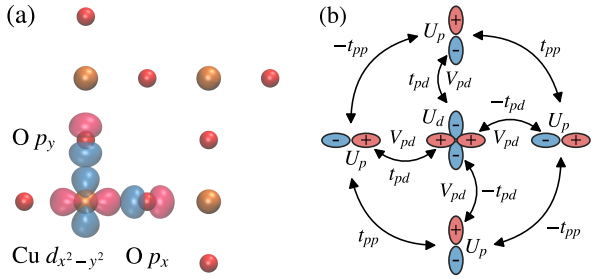

FIG. 1. An illustration of the three-band Hubbard model: (a) the symmetric cluster used in the DMET calculations, where the orange and red atoms denote copper and oxygen respectively; (b) definition of the model parameters and the phase convention.

As a minimal atomic model of the CuO_2 layer in cuprates, the three-band model describes the on-site and nearest-neighbor interactions among the Cu $d_{x^2-y^2}$ and O p_x, p_y orbitals [see Fig. 1(a)]. In the hole representation, the Hamiltonian reads,

$$\begin{aligned}\mathcal{H} = {} & t_{pd} \sum_{\langle ij\rangle\sigma} \left(d^\dagger_{i\sigma} p_{j\sigma} + \text{H.c.} \right) + t_{pp} \sum_{\langle jj'\rangle\sigma} \left(p^\dagger_{j\sigma} p_{j'\sigma} + \text{H.c.} \right) \\ & - \Delta_{pd} \sum_{i\sigma} n^d_{i\sigma} + U_d \sum_i n^d_{i\alpha} n^d_{i\beta} + U_p \sum_j n^p_{j\alpha} n^p_{j\beta} \\ & + V_{pd} \sum_{\langle ij\rangle\sigma\sigma'} n^d_{i\sigma} n^p_{j\sigma'},\end{aligned} \tag{1}$$

where $\langle \cdots \rangle$ denotes nearest neighbors, $d^{(\dagger)}_{i\sigma}$ and $p^{(\dagger)}_{j\sigma}$ destroy (create) a hole with spin σ ($\in \{\alpha, \beta\}$) on the Cu d and O p orbitals respectively, $n^d_{i\sigma}$ and $n^p_{j\sigma}$ are the corresponding hole particle-number operators, and the charge transfer gap Δ_{pd} is defined as the orbital energy difference, $\epsilon_p - \epsilon_d$. Similarly to in the one-band Hubbard model, the hopping term and on-site Coulomb repulsion will be denoted t and U, and the Coulomb interaction between nearest-neighbor p, d orbitals will be denoted V_{pd}. Note that the hopping term involves a phase factor (± 1) introduced by the choice of orbital orientation in the basis as shown in Fig. 1(b).

There has been much work to determine the parameters of the three-band model; however, a consensus set does not exist [32, 54–57]. There has been particular debate about the size of the charge transfer gap Δ_{pd} [32, 58].

TABLE I. Parameters of the three-band Hubbard model used in this work, in units of eV. The parameters correspond to the hole representation.

Model	t_{pd}	Δ_{pd}	U_d	t_{pp}	U_p	V_{pd}
Hybertsen[a]	1.3	3.6	10.5			
Martin[b]	1.8	5.4	16.5			
Hanke[c]	1.5	4.5	12.0			
Hanke full[c]	1.5	4.5	12.0	0.75	5.25	0.75

[a] From Ref. [54].
[b] From Ref. [56].
[c] From Ref. [37].

In this work, we consider four sets of published model parameters, see Table I, as well as the sensitivity of orders to changing these parameters. Note that all parameter sets are given in eV, thus all energies in this work are reported in units of eV unless otherwise specified. The first three sets include only the most essential terms, i.e., t_{pd}, U_d and Δ_{pd}, and thus we refer to them as *minimal* parametrizations. When normalized to units of t_{pd}, the other parameters vary within a range of 10%. The fourth set involves all terms in Eq. (1). We refer to this as a *full* parametrization. In the hole representation, the minimal parametrization is equivalent to the full model with t_{pp}, U_p and V_{pd} set to zero.

B. Computational formulation

1. Framework

DMET approximates the expectation values in the interacting lattice by those in a quantum impurity model. The impurity model is solved simultaneously with a fictitious non-interacting lattice problem, whose ground state defines the bath sites of the impurity model via a Schmidt decomposition [38, 59]. Self-consistency is achieved by matching the one-particle density matrix of the impurity model and non-interacting lattice ground states via a *correlation potential* u applied to the non-interacting lattice. The basic steps of the DMET self-consistency loop are thus (a) compute the ground state of the non-interacting lattice Hamiltonian with correlation potential u, (b) construct the bath sites and impurity model Hamiltonian, (c) solve for the ground state of the impurity model, and (d) match the one-particle density matrices of the lattice Hamiltonian and impurity model to update u. The cycle ends when the correlation potential u is converged.

In this work, we are interested in both magnetic and superconducting phases. Consequently, the correlation potential takes the form

$$u = \sum_{ij\sigma} v_{ij}^{\sigma} a_{i\sigma}^{\dagger} a_{j\sigma} + \sum_{ij} \Delta_{ij}^{\alpha\beta} a_{i\alpha}^{\dagger} a_{j\beta}^{\dagger} + \text{H.c.}, \tag{2}$$

where optimizing over v^{σ} and $\Delta^{\alpha\beta}$ in the self-consistency procedure allows for formation of spin polarized and singlet superconducting pairing (between two spin channels α and β) order in the lattice and impurity problems. The non-interacting lattice Hamiltonian is then of Bogoliubov-de Gennes form [60]. The corresponding ground-state solution is a mean-field Bardeen-Cooper-Schrieffer (BCS) wavefunction, and a set of bath orbitals that describes the environment can be constructed from the corresponding generalized density matrix. The detailed formulas for the bath construction are summarized in Appendix A and the integral transformation expressions for the BCS mean field can be found in Refs. [40, 61]. These routines have been implemented in libDMET [62, 63].

2. *Impurity and lattice*

We used a 2×2 impurity cluster of CuO_2 primitive cells [37] which retains the inversion and four-fold rotation symmetry of the lattice [see Fig 1(a)]. We embedded the cluster in a 20×20 unit-cell (40×40 site-length) lattice. We performed DMET calculations for dopings x ranging between -0.8 and 0.8 (negative denotes electron doping and positive denotes hole doping). Unless otherwise specified, we initialized u with an antiferromagnetic guess and a random pairing potential.

3. *Impurity Hamiltonian and solver*

The impurity model Hamiltonian was constructed using the non-interacting DMET bath formalism [38, 40], and the ground state was determined using a density matrix renormalization group (DMRG) solver [64, 65], allowing for particle number symmetry breaking and spin polarization [40]. During the DMET self-consistent cycle we used a maximum bond dimension $M = 800$. Subsequent bond dimension convergence checks were performed using (up to) $M = 2000$. To minimize entanglement and ensure a small bond dimension M in the ground state, we rotated the impurity Hamiltonian into a basis of split-localized molecular orbitals (MOs) obtained from the self-consistent Hartree-Fock-Bogoliubov (HFB) method, where the occupied and virtual MOs were computed using the PySCF package [66, 67], and the occupied and virtual spaces were subsequently localized separately using the Edmiston-Ruedenberg procedure that maximizes the Coulomb energy of each orbital [68, 69]. The standard genetic algorithm implemented in the Block program [69–72] was used to order the orbitals for the DMRG calculation. The tolerance of the DMRG sweep energy was set to 10^{-6}. Convergence checks on the accuracy of DMRG energies are described in Appendix C.

4. *DMET self-consistency*

We carried out DMET self-consistency using full impurity-bath fitting [40, 44], where the cost function measures the least-squares difference between the correlated one-particle density matrix γ^{corr} and the non-interacting lattice density matrix projected to the full impurity problem γ^{mf},

$$w(u) = \sum_{kl}^{\text{imp+bath}} \left[\gamma_{kl}^{\text{mf}}(u) - \gamma_{kl}^{\text{corr}}\right]^2. \tag{3}$$

We minimized w using a conjugate gradient (CG) minimizer with line search. Since the gap of the non-interacting lattice model is often small (in the case of doped systems), a finite inverse temperature $\beta = 1000\, t_{pd}$ was used to define the non-interacting density matrix to ensure smooth convergence (see Appendix B for further discussion and expressions for the analytic gradient of the cost function at finite temperature). We matched the particle number on the impurity sites and on the lattice exactly by separately fitting the chemical potential using quadratic interpolation [61]. Direct inversion in the iterative subspace (DIIS) [73, 74] was employed to accelerate the overall DMET convergence, using the difference of u between two adjacent iterations as the error vector. We chose the convergence threshold to be 10^{-4} in the correlation potential u (per site), which we observed to translate to an energy convergence per site of better than 10^{-4}. We further analyze the numerical convergence and error estimates for the DMET self-consistency in Appendix C.

5. *Order parameters*

To characterize the doping dependence of the ground-state, we define average AFM and d-wave SC order parameters. As usual, the AFM order parameter is chosen as the staggered magnetization,

$$m_{\text{AFM}} = \frac{1}{4} \sum_{i \in \text{Cu}} \eta_i^{\text{AFM}} m_i^d, \tag{4}$$

where m_i^d is the local magnetic moment on a Cu-d orbital, $\frac{1}{2}\left(n_{i\alpha}^d - n_{i\beta}^d\right)$, and the η^{AFM} is the local structure factor,

$$\eta_i^{\text{AFM}} = \begin{cases} +1, \text{ if } n_{i\alpha}^d \geqslant n_{i\beta}^d, \\ -1, \text{ if } n_{i\alpha}^d < n_{i\beta}^d. \end{cases} \tag{5}$$

The SC order parameter here is evaluated as the average of the Cu-Cu and O-O d-wave pairing components,

$$\begin{aligned} m_{\text{SC}} = &\sum_{\langle ii' \rangle} \frac{1}{\sqrt{2}} \eta_{ii'}^{\text{SC}} \left(\left\langle d_{i\alpha} d_{i'\beta} \right\rangle + \left\langle d_{i'\alpha} d_{i\beta} \right\rangle\right) \\ &+ \sum_{\langle\langle jj' \rangle\rangle} \frac{1}{\sqrt{2}} \eta_{jj'}^{\text{SC}} \left(\left\langle p_{j\alpha} p_{j'\beta} \right\rangle + \left\langle p_{j'\alpha} p_{j\beta} \right\rangle\right), \end{aligned} \tag{6}$$

where $\langle \cdots \rangle$ limits the summation such that only the pairing between nearest Cu-d orbitals is taken into account, and similarly $\langle\langle \cdots \rangle\rangle$ involves only the next-nearest coupling between

O-p orbitals. The d-wave superconducting structure factor η^{SC} is defined as,

$$\eta^{\mathrm{SC}}_{ii'} = \begin{cases} +1, \text{ if } \mathbf{R}_i - \mathbf{R}_{i'} = \pm\mathbf{e}_x, \\ -1, \text{ if } \mathbf{R}_i - \mathbf{R}_{i'} = \pm\mathbf{e}_y. \end{cases} \quad (7)$$

III. THE THREE-BAND PHASE DIAGRAM

A. Undoped state

TABLE II. Charge, spin distribution (magnetic moments) and energy gap of the undoped three-band Hubbard model and reference data. Note that the experimental gaps reported are all optical gaps.

Model	ρ_{Cu}	ρ_{O}	m_{Cu}	m_{O}	E_{g} [eV]
Hybertsen	1.238	1.881	0.363	0.000	2.5
Martin	1.219	1.891	0.375	0.001	4.4
Hanke	1.220	1.890	0.373	0.000	3.9
Hanke full	1.358	1.821	0.279	0.002	2.2
Others	1.23[a]	1.89[a]	0.29[b], 0.31[c]		2.25[b],
Cuprate			0.3 ± 0.025[d]		1.5-2.0[e], 1.5-1.7[f]

[a] DMRG result from Ref. [26], using a similar model to Hanke full (with a different $U_p = 4.5$, $V_{pd} = 1.5$ and $V_{pp} = 1.125$).
[b] VCA result from Ref. [36], using basically the same model as Hanke full (with a different $U_p = 4.5$).
[c] VCA result from Ref. [37], using the same model as Hanke full.
[d] Experimental result for La_2CuO_4, from Ref. [75].
[e] Experimental result for La_2CuO_4, from Refs. [76–78].
[f] Experimental result for $YBa_2Cu_3O_6$, from Refs. [77, 79].

1. Charge and magnetic moments

We present the order parameters for the undoped state from DMET and from reference calculations and experimental measurements in Table II. As expected, the d orbitals are roughly half-filled and the p orbitals are roughly doubly occupied, with some charge transfer between the two due to hybridization. Comparing the full and minimal parametrizations, in the full parametrization, the Cu site is more strongly occupied by electrons, due to the t_{pp} term which smears out the oxygen charge and effectively transfers it to copper (while the effect of U_p is very small, see the discussion in Sec. III B). Unlike on the O site, the spin density on the Cu site is polarized, with a large local magnetic moment, which compares well to the experimental value 0.3 ± 0.025 μ_{B} (0.6 ± 0.05 μ_{B}) [75], as well as previously computed theoretical moments of 0.29 [36] and 0.31 [36] from VCA. In addition, the magnetic moment in the full parametrization is reduced relative to the minimal parametrizations, because the increased electron density on copper dilutes the polarized spin, while the additional holes on oxygen reduce the strength of the super-exchange-based antiferromagnetic coupling. In fact, the local magnetic moments in the minimal models appear to be too large, while that of the full model is similar to experimental results. However, it is also known from one-band calculations, that the magnetic moments are overestimated in 2×2 DMET clusters relative to the thermodynamic limit (e.g., by about 25% at $U = 6$, see Fig. S1 in the Supplemental Material [80]. Assuming similar finite size errors, then the minimal parametrization may provide reasonable magnetic moments at half-filling in the thermodynamic limit (although this is not necessarily the case under doping, see below).

2. Band gap

As a simple estimate of the single-particle gap, we also computed the energy gap of the converged DMET non-interacting lattice Hamiltonian (DMET NI gap), i.e. $E_{\mathrm{g}} = \varepsilon_{\mathrm{CBM}} - \varepsilon_{\mathrm{VBM}}$, where C(V)BM denotes conduction (valence) band minimum (maximum). Note that although the charge and spin densities in the different parametrizations are generally similar, the DMET NI gap varies more significantly, from 2.2 to 4.4 eV. The Hybertsen and Hanke parameter sets were derived from calculations on La_2CuO_4 (LCO), where the optical energy gap is variously reported as lying in the range 1.5 to 2.0 eV [76–78] (note that the optical gap is generally smaller than the fundamental gap). The estimated DMET NI gap of 2.5 and 2.2 eV for the Hybertsen and Hanke full parameter set respectively are thus in reasonable agreement with the experimental gap. However, the minimal Hanke parametrization seriously overestimates the gap. The Martin parameter set, obtained from calculations on finite-sized Cu-O clusters, are all systematically larger than in the other sets, and thus give the largest DMET NI gap. However, since the ratio of parameters in the Martin model remains similar to other parametrizations (and thus give rise to similar charge and spin distributions) this suggests that all energy parameters in the Martin model should simply be simultaneously rescaled downwards.

3. Orbital resolved band structure

Unlike in the one-band Hubbard model, where the insulating gap arises between Hubbard bands, the gap in correlated insulators in the three-band model can arise from both Hubbard and charge-transfer mechanisms. In Fig. 2, we plot the projected electronic band structure and density of states from the DMET non-interacting lattice Hamiltonian, as converged for the fully parametrized Hanke model. The CBM is mainly of Cu d character (upper Hubbard band), while the VBM shows mixed character, dominated somewhat by O-p. The mixed orbital character of the valence bands around the Fermi level is consistent with the Zhang-Rice singlet (ZRS) hypothesis [4], in which hybridization between oxygen and copper orbitals induces superexchange that leads to singlets of O and Cu holes. Further support for the ZRS picture comes from the $\mathbf{k}$-dependent orbital weights; that of Cu-d is greater at the Γ point, while that of O-p is larger at the M point, consistent with earlier model analysis of the ZRS state [81] and results from VCA [36]. In total, these observations indicate that the undoped three-band model ground state is a charge transfer insulator, with mainly a p-d type energy gap (see Ref.

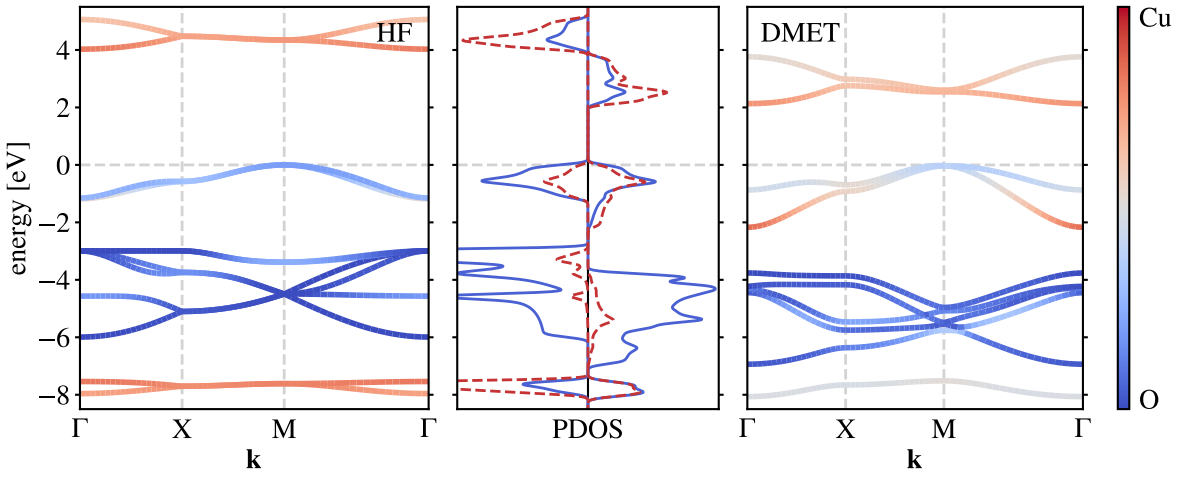

FIG. 2. Orbital-projected electronic band structure and density of states (PDOS) of the undoped three-band Hubbard model with Hanke full parameters from HF (left) and DMET (right). The special **k** points [Γ: $(0,0)$, X: $(\pi,0)$, M: (π,π)] are in the first Brillouin zone of the 2×2 supercell lattice. The valence band maximum (VBM) is chosen as the energy zero.

[82] for experimental evidence of the charge-transfer nature of the band gap). The strong **k**-dependent hybridization clearly poses challenges for numerical downfolding techniques to a one-band picture.

Comparing the DMET NI band structure to the Hartree-Fock mean-field description (also shown in Fig. 2), we find that the HF gap (≈ 4 eV) is significantly overestimated, and the d-p hybridization is significantly weaker, resulting in a VBM with dominant oxygen p character and very narrow dispersion. Thus the reduced gap and d-p hybridization, both seen in experiment, are fluctuation driven phenomena, whose average effect is being captured by the DMET correlation potential u.

B. Doped states

1. *Hole doped phases with standard parametrizations*

More interesting ground states, including those with superconducting order, appear under doping. An important difference with the one-band case is the asymmetry of the three-band model under doping. We first focus on the orders that appear under hole-doping. Although our calculations are all at zero temperature, we can loosely identify the magnitude of the order parameters with transition temperatures in the phase diagram, thus allowing us to compare them to the experimental phase diagram. In Fig. 3, we plot the AFM and d-wave SC order parameters of the Hanke model as a function of hole doping (Hybertsen and Martin minimal model results are very similar to those of the Hanke minimal model, as shown in Fig. S2 of the Supplemental Material [80]). In the fully parametrized model, we find two different solutions of the DMET self-consistency, labelled solution 1 (obtained from a weakly spin polarized AFM guess) and solution 2 (obtained from a strongly polarized AFM guess).

For all parameter sets, we observe that the AFM order parameter decreases as doping increases, consistent with the general behavior of the cuprate phase diagram [82]. However, for the minimal models, the AFM order persists even up to large dopings (e.g. ≈ 0.15 at $x = 0.3$). In interpreting this discrepancy, one complication is that computation is measuring atomic scale local order, while experimental measurements are likely averages over various inhomogeneities (e.g. different orientations of stripes in different layers) which would typically lead to reduced moments. Leaving this aside, however, the overestimation of the computed moment could originate either from the remaining finite size error in the DMET calculation, or from the unphysical nature of the parametrization (e.g. the lack of doping dependence of the parameters). From

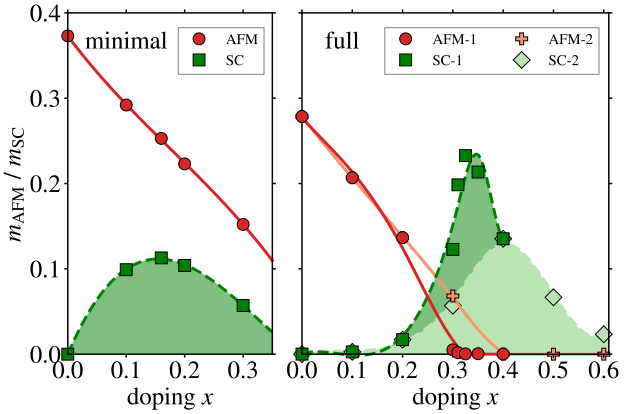

FIG. 3. Antiferromagnetic and d-wave superconducting order parameters of the hole-doped three-band Hubbard model. The model settings are from the Hanke minimal (left) and Hanke full (right) parameter sets. Note that in the "Hanke full" case, we find two possible solutions between $x = 0.2$ and $x = 0.4$, marked as solution "1" (from a weakly polarized AFM guess) and "2" (from a strongly polarized AFM guess) in the figure. The curves are cubic-spline interpolated.

our earlier work on the one-band Hubbard model [40], we know that DMET calculations using a 2×2 impurity (e.g. in the range $U/t = 6 - 8$) indeed overmagnetize not only at half-filling but also in the doped regime (see Fig. S1 of the Supplemental Material [80]). However, the one-band AFM order nonetheless vanishes at dopings larger than 0.25, more rapidly than what we observe in the minimal parametrized three-band model. In addition, the full parametrization of the three-band model also predicts a more realistic trend for the AFM order at large doping. Taken together, this suggests that the observed persistent AFM order is likely due to the over-simplified minimal model parameters. Although the AFM order in the full model does decrease to zero in the observed doping range, it vanishes between $x = 0.2$ and 0.3 (more similar to the one-band model). This is beyond the experimental boundary for the pure AFM phase ($x < 0.1$), but close to the boundary of the pseudogap region [83, 84]. Like in the one-band model, we would expect longer wavelength orders (such as striped phases [7, 40]) to appear in this region with larger computational clusters.

From Figs. 3 and S2, we see that d-wave superconducting order (coexisting with antiferromagnetism) appears in the phase diagram of all parameter sets. (Discussion of additional pairing orders, as well as comparisons to the one-band model can be found further below). In the minimal models, the d-wave pairing reaches a maximum at around $x = 0.15 - 0.20$.

As a result of the overestimation of AFM order discussed above, the minimal models show coexistence of AFM + SC order for all the studied dopings. However, in the full parametrization, the two coexist in the range 0.1 to 0.4 (for solution 2), and 0.1 to 0.3 (for solution 1), with d-wave order reaching a maximum near $x \approx 0.30 - 0.35$, somewhat larger than seen in experiments (≈ 0.15 - 0.2) [75]. Solutions 1 and 2 coincide for $x < 0.2$ and $x > 0.4$ but are distinct in between, reflecting the known competition between orders at intermediate doping [84]; solution 1 is slightly lower in energy and displays significantly stronger superconducting order. Note that it is also possible to converge a paramagnetic SC solution (by constraining the correlation potential in Eq. 2 so that $v^\alpha = v^\beta$ and $\Delta = \Delta^\dagger$). In this case, the SC order is already evident at $x = 0.1$, since the AFM order is artificially suppressed. However, the energy of this paramagnetic state is much higher than the AFM + SC states we have discussed, and is unstable if one releases the constraints on the potential. We thus believe the coexistence of AFM and SC order to be a true feature of the three-band model ground state, as has also been observed in VCA studies [36, 37].

2. *Range of reasonable parameters*

In view of the significant differences between the minimal and full parametrizations, we now examine more deeply how individual parameters influence the phase diagram. To do so, we change the individual parameters appearing in the Hanke minimal model, and restrict ourselves to the magnetic order for simplicity. We compare the magnetic phase diagram computed using both Hartree-Fock and DMET. While the mean-field Hartree-Fock method overestimates the magnetic moments, and the resulting AFM domes always lie above the DMET ones in the plots, it should be noted that parametrizations are often derived from mean-field calculations. Thus the difference in sensitivity between DMET and HF to the model parameters gives some insight into the sizes of errors arising from mean-field parametrization schemes.

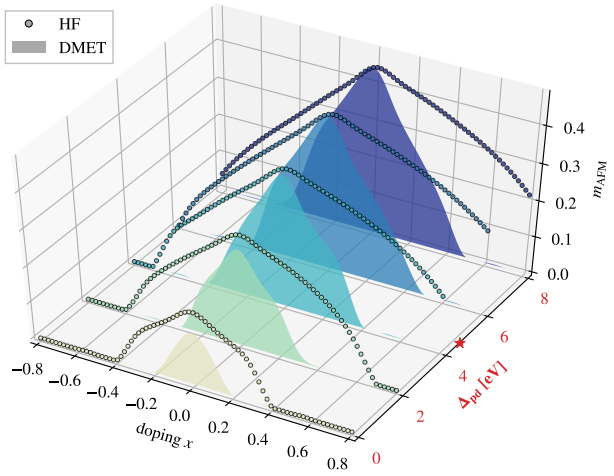

FIG. 4. Effects of Δ_{pd} on the magnetic phase diagram of the three-band Hubbard model. Δ_{pd} ranges from 0.0 to 8.0 eV and the star marker labels the value used in the Hanke model (4.5 eV). Both Hartree-Fock (dotted line) and DMET (shaded area) results are shown.

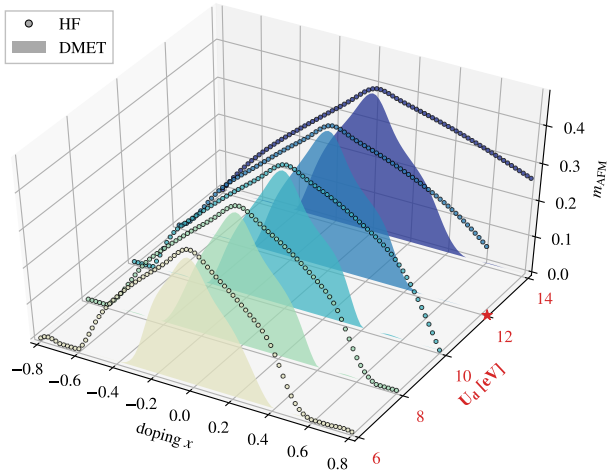

FIG. 5. Effects of U_d on the magnetic phase diagram of the three-band Hubbard model. U_d ranges from 6.0 to 14.0 eV and the star marker labels the value used in the Hanke model (12.0 eV). Both Hartree-Fock (dotted line) and DMET (shaded area) results are shown.

We first study the influence of Δ_{pd}, whose value is uncertain in the literature [32, 58]; the magnetic phase diagram computed using both Hartree-Fock and DMET is shown in Fig. 4. On the hole-doped side, when $\Delta_{pd} \geqslant 4$ eV, the HF magnetic moment does not vanish even at a large doping of $x \approx 0.8$, while in contrast, DMET always predicts a finite

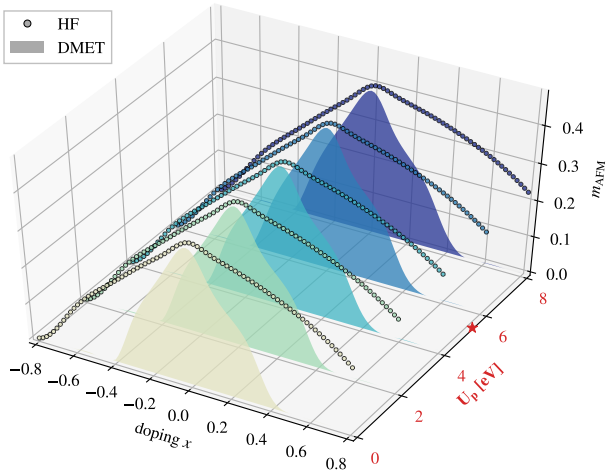

FIG. 6. Effects of U_p on the magnetic phase diagram of the three-band Hubbard model. U_p ranges from 0.0 to 8.0 eV and the star marker labels the value used in the Hanke full model (5.25 eV). Both Hartree-Fock (dotted line) and DMET (shaded area) results are shown.

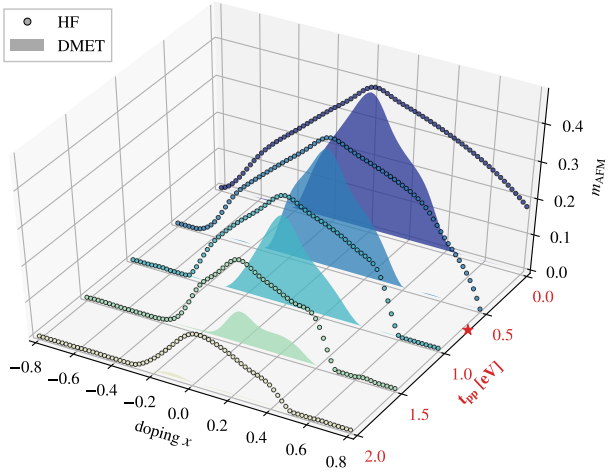

FIG. 7. Effects of t_{pp} on the magnetic phase diagram of the three-band Hubbard model. t_{pp} ranges from 0.0 to 2.0 eV and the star marker labels the value used in the Hanke full model (0.75 eV). Both Hartree-Fock (dotted line) and DMET (shaded area) results are shown.

AFM region with a sharp peak at $x = 0$. The DMET magnetic moment m_{AFM} increases monotonically from 0.14 to 0.44 as we increase Δ_{pd}, which can be understood from second-order perturbation theory: The effective d-d hopping $t_{dd} \propto \frac{t_{pd}^2}{\Delta_{pd}}$, thus a larger Δ_{pd} gives a smaller t_{dd} and thus enhances the magnetic moment. Along with the larger moments, the critical doping point where $m_{\mathrm{AFM}} \to 0$ shifts to larger doping as Δ_{pd} increases. Given that, even accounting for finite cluster errors (see above), the minimal model appears to overestimate the magnetic moment under doping and the critical doping concentration, these results suggest one should renormalize Δ_{pd} to smaller values, around 2-3 eV. Finally, we see that the asymmetry with respect to electron and hole doping becomes more pronounced when Δ_{pd} increases, and the magnetic moment is less sensitive to hole doping rather than electron doping. Thus, the appropriate value of Δ_{pd} should neither be too small (as the AFM order as well as doping asymmetry will both be too weak, see also Ref. [32] for a discussion of the unphysical behavior with small Δ_{pd}) nor too large (m_{AFM} order will be too strong to be suppressed by doping, especially on the hole doped side). Ref. [34] suggests a range (1.2 - 2.6 eV) of Δ_{pd} for cuprates, which overlaps the range of our estimates.

We next check the effect of on-site Coulomb repulsion terms. The moment versus U_d is shown in Fig. 5. Unlike Δ_{pd}, the influence of U_d on the shape of the curves is very small, e.g. the undoped DMET m_{AFM} only increases from 0.35 to 0.38 when U_d varies from 6 to 14 eV. The influence on the curve shape is more significant for HF than it is for DMET. In the one-band Hubbard model, however, the situation is very different, where m_{AFM} increases substantially as U is increased [40]. This observation supports viewing the three-band model as primarily a *charge transfer insulator* (and thus less sensitive to the change in the on-site Coulomb U_d), rather than a Mott insulator, whose magnetic moment is directly mediated by U. The situation for the on-site Coulomb repulsion U_p (see Fig. 6) is very similar to that for U_d: the undoped DMET m_{AFM} only increases from 0.37 to 0.38 as U_d varies from 0 to 8 eV, and the HF curves show a similarly weak sensitivity.

We finally study the effect of nearest neighbor oxygen hopping t_{pp} (see Fig. 7). From the figure, we see that the AFM order is effectively frustrated by large t_{pp}, similar to the effect of t' in the one-band Hubbard model. It has been shown in Ref. [32] that t_{pp} can vary substantially for different cuprates (unlike t_{pd}, which is almost unchanged between materials). Our results here suggest that a reasonable range for this parameter is around 0.5 - 1.0 eV; too large a t_{pp} will suppress the AFM order.

Overall, we find that the magnetic phase diagram is sensitive to Δ_{pd} and t_{pp}, but not to U_d and U_p. The improved results of the full model are thus likely due to the introduction of t_{pp}, rather than U_p. In particular, if we wish to have a reasonable description of the three-band Hubbard model within a minimal set of parameters, Δ_{pd} should be renormalized to a smaller value to take the effect of t_{pp} into account. The Hanke parametrization of the full model yields more physical results, and thus we will only use this full model in the remainder of the discussion. However, we note that it is still not optimal with respect to choosing values of Δ_{pd} and t_{pp} that match experiment. This may in part be due to the mean-field derivation of some of the parameters.

3. *Electron doped phases in the full model*

We now turn to the electron doped orders, which as mentioned above, are different from the hole-doped orders, unlike in the one-band model [26, 84]. We show the AFM and SC order versus both hole and electron doping in Fig. 8 (the hole doped side corresponds to solution 1 in Fig. 3). As we dope with more electrons, the AFM order diminishes. The critical

doping x_c that makes m_{AFM} vanish (0.15 - 0.20) is smaller than that on the hole doped side. This is quite different from what is seen in experiment: the commonly accepted cuprate phase diagram typically shows a sudden drop of AFM order on the hole doped side [82], with a larger region of coexistence on the electron doped side. This likely reflects the fact that a single parameter set does not describe the electron-doped and hole-doped materials equally well.

For the SC phase, the overall d-wave pairing magnitude is smaller in the electron doped region, similar to the lower T_cs seen in experiment. Also, the SC phase on the electron doped side has an interesting "M" shaped two-peak structure: The d-wave SC order increases first with respect to the doping, but decays to a small value around the AFM critical x_c, before growing to another peak after the AFM order vanishes. The first peak around $x = 0.05$ is very similar in shape to the peak in DMET calculations of the one-band Hubbard model, where the SC order emerges immediately after doping (see the lower panel of Fig. 8). The second peak, occurring after the disappearance of the AFM order, is similar to the hole doped SC peak. The presence of two qualitatively different SC phases may be a hint of the types of competing orders that can arise on the electron-doped side, which to date have not been much investigated in numerical studies.

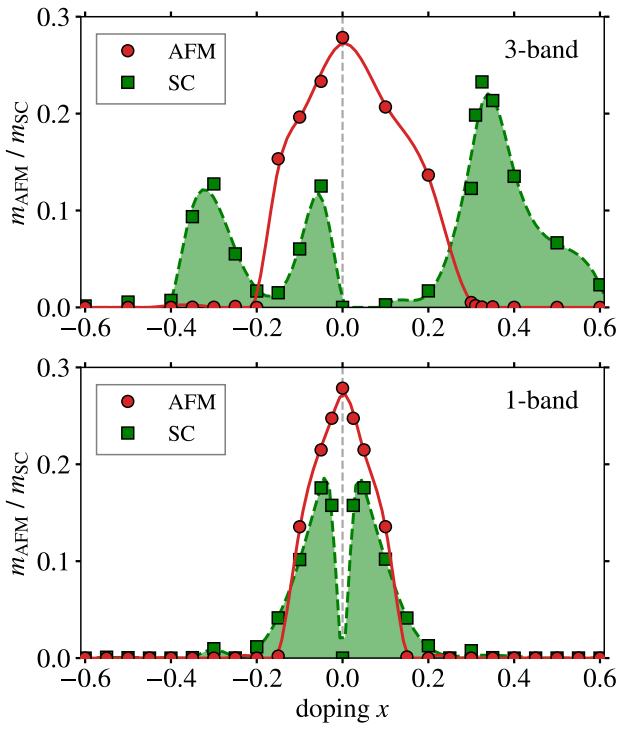

FIG. 8. Comparison of electron doped ($x < 0$) and hole doped ($x > 0$) orders. Upper panel: AFM and SC order of the three-band Hubbard model (Hanke full parameter set). Lower panel: AFM and SC order of the one-band Hubbard model (2×2 DMET cluster), with U fitted such that at $x = 0$, m_{AFM} is the same as that of the three-band model.

4. *Atomic scale orders in the full model*

Beyond the bulk order parameters, the three-band model and the explicit inclusion of both copper and oxygen atoms into the DMET impurity cluster allows for the possibility of studying the magnetic and superconducting order at the atomic scale. The explicit charge, spin, and pairing orders are shown in Fig. 9. We only present representative results from the Hanke full model at $x = 0.0$, $x = 0.3$ (solution 1) and $x = -0.3$ doping, since the results from other parametrizations and dopings are qualitatively similar. (Further plots are presented in Figs. S3 - S8 of the Supplemental Material [80]). Comparing Figs. 9(a) and 9(b), we see that on doping the holes mainly occupy the oxygen sites and the hole density on copper only increases slightly. Combined with the fact that doped electrons mainly reside on Cu [see Fig. 9(e), the hole density on Cu is reduced], this reflects the particle-hole asymmetry of the three-band model [26, 84]. With respect to pairing order, we see $d_{x^2-y^2}$-wave symmetry clearly between neighboring Cu sites (i.e. it transforms according to the B-representation of the C_4 group and the sign of the pairing changes on rotating by 90°), see Figs. 9(b) and 9(e). The Cu-Cu pairing order is the largest pairing order between the atoms. From Figs. 9(c) and 9(f), we also see d-wave order between the *next-nearest* O p orbitals. Although the magnitude is slightly smaller than that of the Cu-Cu pairing, it still contributes almost $\approx 20\% - 40\%$ of the bulk d-wave order in Eq. (6). We note that the O-O pairing contribution is also asymmetric with respect to doping. In particular, its contribution can be as large as $\approx 40\%$ in the hole doped side but only 20-30% in the electron doped region. Finally, we consider the pairing order between Cu-O and the nearest O-O atoms, see Figs. 9(d) and 9(g). We see that the coupling between the nearest O-O atoms has s-wave symmetry but is quite weak, related to the incompatible orbital orientations. On the other hand, we find the pairing between Cu-O to be relatively strong (in all parameter sets). The local symmetry of Cu-O coupling has $p_{x(y)}$-wave [or $d_{xy(yz)}$-wave] symmetry (the pattern transforms according to the E-representation of the C_4 group), which to our knowledge has not previously been reported. We note that the superconducting phase pattern between Cu and O is similar to the orbital current-current correlation patterns in Ref. [13], although the current-current correlations were reported to be extremely weak. The pattern is also similar to the asymmetry reported as a hidden order in polarized elastic neutron diffraction experiments [8]. Further investigation of these and other intriguing connections to intracell orders is left to future work.

IV. CONCLUSIONS

In summary, we have used density matrix embedding theory to characterize the ground-state phases of the three-band Hubbard model. We have calculated the charge, local magnetic moments, projected energy bands and density of states of the undoped three-band model, which support a charge-transfer insulating character at zero doping.

We also studied the doping dependence of the ground-state

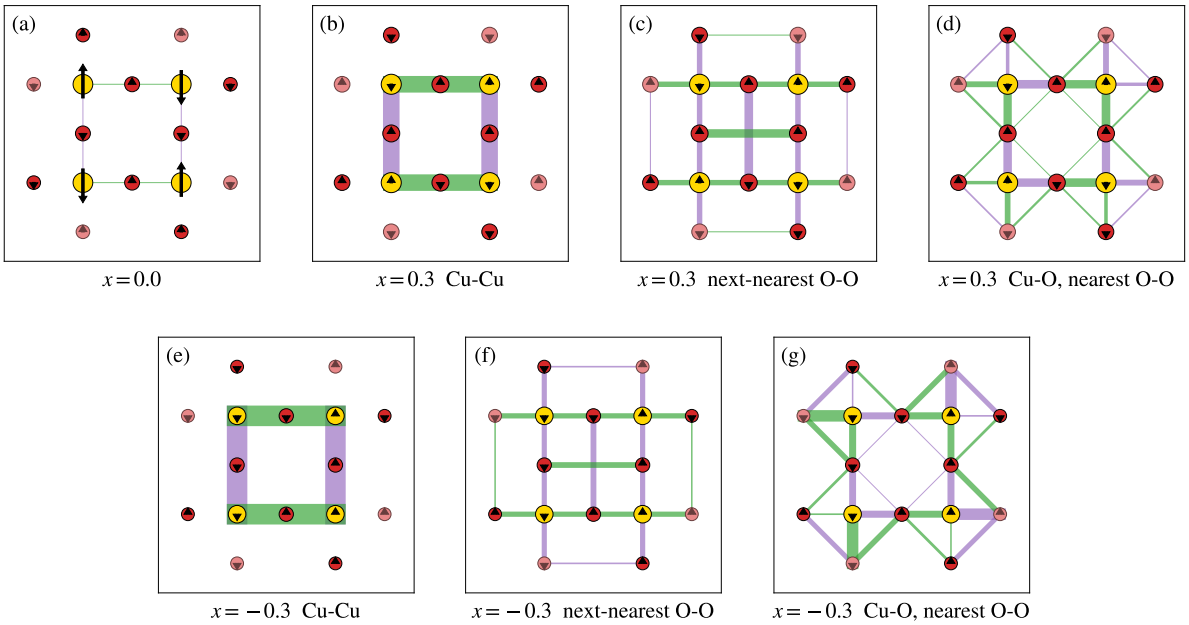

FIG. 9. Charge, spin and pairing orders in the three-band Hubbard model. We use yellow and red circles for Cu and O respectively. The area of the circle reflects the corresponding local hole density, the length of the arrow denotes the magnitude of the local magnetic moment, the width of the lines is proportional to the pairing strength and different colors of the lines denote different coupling signs. The results are calculated based on the fully parametrized model at $x = 0.0$ [(a)], $x = 0.3$ doping [solution 1, (b) - (d)] and $x = -0.3$ doping [(e) - (g)]. (b) and (e) show the pairing strength between Cu and Cu; (c) and (f) show the pairing strength between the next nearest neighbor O; (d) and (g) illustrate the couplings of both the nearest Cu-O, and the nearest O-O.

(phase diagram) of the model paying particular attention to the local antiferromagnetic (AFM) and superconducting (SC) orders. In a broad range of model parameters we find a decrease in AFM order upon doping and a SC dome. Unlike in the one-band picture, the models all predict a large region of coexistence of AFM + SC orders, with the AFM order decreasing quite slowly. Comparison to experimental data and earlier theoretical studies suggests that the minimal parametrized models overestimate the AFM order and lead to poorer energy gaps, relative to the full parametrizations, which also include oxygen and oxygen-copper Coulomb repulsion, and oxygen-oxygen hopping. The magnetic moment is particularly sensitive to the Δ_{pd} and t_{pp} parameters, and in the minimal model, the charge transfer gap Δ_{pd} should be renormalized downwards to better capture the experimental phase diagram. Within the full model, there are qualitative differences between the SC orders on the hole- and electron-doped side, with the electron-doped side supporting two different SC domes, one of which appears more similar to the one observed in the one-band model, and the other like the SC dome observed on the hole-doped side.

The three-band model further allowed us to study order at the atomic scale. In the SC region, we observed strong d-wave pairing between Cu-Cu and the next-nearest O-O, weak extended s-wave coupling between the nearest O-O atoms, and p- (or d_{xz}, d_{yz})-like symmetry pairing between Cu-O. The intriguing symmetry of the latter order, similar to that seen in some experiments, illustrates the new physics that emerges at atomic length-scales in the three-band model. Exploring such physics in more detail will be the subject of future work.

ACKNOWLEDGMENTS

We thank Alec White, Nai-Chang Yeh, Patrick Lee, Tianyu Zhu and Yang Gao for helpful discussions. Z.-H.C. thanks Zhiao Yu for help on graphics. This work was supported by the US Department of Energy, Office of Science, via award No. 19390. G.K.C. is a Simons Investigator in Physics and is supported by the Simons Collaboration on the Many-Electron Problem.

Appendix A: DMET Bath Construction

Given a Slater determinant lattice mean-field wavefunction Φ^{HF}, the DMET bath orbitals can be constructed in several equivalent ways, e.g. via a singular value decomposition (SVD) of the MO coefficients [38] or the environment-impurity part of the density matrix [41], or via eigenvalue decomposition of the projected overlap matrix [43] or environment-environment block of the density matrix [44]. All these methods define a set of bath orbitals, which has non-zero overlap with the impurity sites. In this work, we use SVD of the environment-impurity block of the density matrix to efficiently construct the bath in a periodic lattice system [41, 47]. By taking the first unit- (or super-) cell as the impurity and the

remaining cells as the environment, the whole density matrix of the lattice is divided into four blocks,

$$\gamma^{\Phi^{\mathrm{HF}}} = \begin{bmatrix} \gamma^{\mathrm{imp-imp}} & \gamma^{\mathrm{imp-env}} \\ \gamma^{\mathrm{env-imp}} & \gamma^{\mathrm{env-env}} \end{bmatrix}, \tag{A1}$$

where $\gamma^{\mathrm{imp-imp}}$ is the density matrix of the first cell, i.e. $\gamma(\mathbf{R} = \mathbf{0})$; while $\gamma^{\mathrm{env-imp}}$ is the coupling density matrix between the first cell and other cells, i.e. $\gamma(\mathbf{R} \neq \mathbf{0})$. These two blocks can be easily computed in periodic systems by a Fourier transform of the density matrix in $\mathbf{k}$-space,

$$\gamma^{\mathbf{R}}_{ij} = \frac{1}{N_{\mathbf{k}}} \sum_{\mathbf{k}} \mathrm{e}^{\mathrm{i}\mathbf{k}\cdot\mathbf{R}} \gamma^{\mathbf{k}}_{ij}, \tag{A2}$$

where $N_{\mathbf{k}}$ is the number of $\mathbf{k}$-points in the first Brillouin zone. The bath can then be computed by SVD of $\gamma^{\mathbf{R}\neq\mathbf{0}}$ [47],

$$\gamma^{\mathbf{R}\neq\mathbf{0}}_{ij} = \sum_{\tilde{i}} B^{\mathbf{R}\neq\mathbf{0}}_{i\tilde{i}} \Lambda_{\tilde{i}\tilde{i}} V^{\dagger}_{\tilde{i}j}, \tag{A3}$$

where B yields the bath orbital coefficients and the singular values Λ measure the entanglement between bath and impurity orbitals. We note that the $\gamma^{\mathrm{imp-env}}$ and $\gamma^{\mathrm{env-env}}$ blocks are not needed for bath construction and in fact, their computation and storage would be prohibitively expensive in a periodic calculation with many $\mathbf{k}$ points. Therefore, using the SVD of $\gamma^{\mathbf{R}\neq\mathbf{0}}$ is more economical ($O(N_{\mathbf{k}} N_{\mathrm{orb}}^3)$ cost) than diagonalizing the $\gamma^{\mathrm{env-env}}$ block.

In addition to the cost, there are two other advantages of using the SVD. First, it is easy to discard the non-coupled bath orbitals, i.e. bath orbitals with (almost) zero singular values. These bath orbitals are essentially core or virtual orbitals, which have little entanglement with the impurity, and they should be removed from the impurity problem for better numerical stability during the DMET self-consistency. Second, when using finite temperature smearing, the idempotency of the lattice mean-field density matrix is slightly broken. Rigorous treatment of finite-temperature requires a large number of bath orbitals than the number of impurity sites [52]. However, the SVD still provides a good first approximation of the finite-temperature bath, especially at low temperatures.

For the superconducting states Φ^{HFB}, the construction of the bath can still be carried out using SVD, but acting on the (env-imp block of) of the generalized density matrix [40],

$$\gamma^{\Phi^{\mathrm{HFB}}} = \begin{bmatrix} \gamma^{\alpha\alpha} & \kappa^{\alpha\beta} \\ \kappa^{\alpha\beta\dagger} & I - \gamma^{\beta\beta T} \end{bmatrix} = \begin{bmatrix} \left\langle a^{\dagger}_{\alpha} a_{\alpha} \right\rangle & \left\langle a_{\beta} a_{\alpha} \right\rangle \\ \left\langle a^{\dagger}_{\alpha} a^{\dagger}_{\beta} \right\rangle & I - \left\langle a^{\dagger}_{\beta} a_{\beta} \right\rangle^{T} \end{bmatrix}, \tag{A4}$$

where the anomalous part of the density matrix κ allows for a non-zero SC order parameter. Within the singlet pairing picture, particles of one spin sector are allowed to couple with holes of the other spin. Therefore, the number of bath orbitals is effectively two times larger than in the normal state DMET.

Appendix B: Analytic gradients of cost function Eq. (3) at finite temperature

Once the gradients of Eq. (3) are obtained, we can utilize efficient gradient-based numerical methods, such as CG or the Broyden-Fletcher-Goldfarb-Shanno (BFGS) algorithm, to optimize the correlation potential. By differentiating Eq. (3) with respect to u_{ij} we have,

$$\frac{\partial w}{\partial u_{ij}} = 2 \sum_{kl} \left(\gamma^{\mathrm{mf}} - \gamma^{\mathrm{corr}} \right)_{kl} \frac{\partial \gamma^{\mathrm{mf}}_{kl}}{\partial u_{ij}}, \tag{B1}$$

and thus the key task in Eq. (B1) is to evaluate the response of the mean-field density matrix with respect to a perturbation, $\partial \gamma^{\mathrm{mf}}_{kl} / \partial u_{ij}$. The response at zero temperature can be written in terms of orbital coefficients and energies (see e.g. Refs. [44, 61]) using first order perturbation theory,

$$\frac{\partial \gamma^{\mathrm{mf}}_{kl}}{\partial u_{ij}} = \sum_{p}^{\mathrm{occ}} \sum_{q}^{\mathrm{virt}} \frac{C_{kp} C^{*}_{lq} C_{iq} C^{*}_{jp} - C_{kq} C^{*}_{lp} C^{*}_{iq} C_{jp}}{\epsilon_p - \epsilon_q}, \tag{B2}$$

where we have assumed the system is *gapped*. However, when the system becomes (nearly) gapless, this expression diverges. In such cases, the divergent gradient causes the optimization to fail, and this is a source of many convergence difficulties in DMET.

One way to ameliorate this issue is to introduce a finite temperature smearing, similar to what is used in mean-field calculations of metals. With an inverse temperature β and a perturbation δu, the Fermi-Dirac density matrix is defined as,

$$\gamma_{kl} = \left[1 + \mathrm{e}^{\beta(h - \mu + \delta u)} \right]^{-1}_{kl}, \tag{B3}$$

where μ is the Fermi level for the (quasi-)particles. The response of γ with respect to the correlation potential u then involves two terms,

$$\frac{\mathrm{d}\gamma_{kl}[u, \mu(u)]}{\mathrm{d}u_{ij}} = \left. \frac{\partial \gamma_{kl}}{\partial u_{ij}} \right|_{\mu} + \frac{\partial \gamma_{kl}}{\partial \mu} \frac{\partial \mu}{\partial u_{ij}}, \tag{B4}$$

where the first term is the direct response of the density at a fixed Fermi level, while the second term reflects the contribution of the implicit change in the Fermi level due to the change in potential. The final expression for the first term in Eq. (B4) is,

$$\frac{\partial \gamma_{kl}}{\partial u_{ij}} = \sum_{pq} C_{kp} C^{*}_{ip} K_{pq} C_{jq} C^{*}_{lq}, \tag{B5}$$

where

$$K_{pq} \equiv n_p (1 - n_q) \frac{1 - \mathrm{e}^{\beta(\varepsilon_p - \varepsilon_q)}}{\varepsilon_p - \varepsilon_q}. \tag{B6}$$

It is easy to check that K_{pq} is always finite when $\varepsilon_p = \varepsilon_q$. One can also let β go to infinity and choose p / q to label occupied / virtual orbitals; the gradient then gives the correct zero temperature limit in Eq. (B2) (up to a symmetrization).

The final expressions for the second term in Eq. (B4) are,

$$\frac{\partial \gamma_{kl}}{\partial \mu} = \sum_p \beta C_{kp} n_p (1-n_p) C^*_{lp},$$
$$\frac{\partial \mu}{\partial u_{ij}} = \left[\sum_p n_p(1-n_p) C^*_{ip} C_{jp}\right] \Big/ \left[\sum_p n_p(1-n_p)\right]. \quad \text{(B7)}$$

Usually this contribution is very small at low temperatures, compared to the direct response in Eq. (B5). However, this contribution will be important in a real finite temperature simulation, e.g. in Ref. [52].

We summarize the derivation of Eqs. (B5) - (B7) in the Supplemental Material [80].

Appendix C: Numerical convergence

Here we assess the accuracy and convergence of the DMET procedure in the three-band model calculations. The error in the DMET calculations arises from three possible sources: (a) DMET self-consistency error (from incomplete convergence), (b) DMRG solver error due to the finite bond dimension, and (c) error from the finite size of the impurity. The finite size error (c) can, in principle, be eliminated by increasing the cluster size and extrapolating to the thermodynamic limit (TDL), as performed in the one-band Hubbard model case [40]. In this work, we use a fixed 2×2 cluster size due to the increased computational cost of the three-band model, and thus we cannot assess the finite-size error, except via some comparisons to the 2×2 cluster error in the one-band model. However, the error due to (a) and (b) can be directly estimated in our framework, which we now discuss.

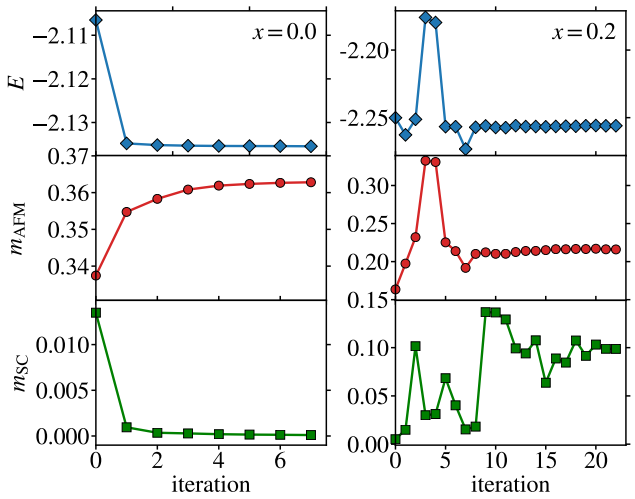

FIG. 10. DMET energy (in units of t_{pd}) and order parameters of the Hybertsen minimal parametrized three-band model, with respect to the number of iterations, at doping $x = 0.0$ (left) and $x = 0.2$ (right).

Fig. 10 shows the overall convergence of DMET with respect to the number of DMET self-consistent iterations. We observe qualitatively different convergence in the normal and superconducting parts of the DMET phase diagram. To illustrate this, we plot the DMET energy, AFM, and (d-wave) SC order parameter for the Hybertsen model at different dopings x. (These order parameters are defined precisely in Sec. II B). We first discuss the undoped system. Here we see that the DMET cycle converges smoothly within 7 iterations. For the DMET energy, a single DMET step is enough to converge to $\approx 10^{-4}$, demonstrating the utility of single-shot DMET calculations in normal (and especially non-magnetic) states. The order parameters (density matrices) are more strongly affected by self-consistency. We find that the AFM order increases during the iterations, while the SC order is suppressed, giving a pure antiferromagnetic state at convergence. We next consider $x = 0.2$ doping. Here, the self-consistency cycle converges more slowly, requiring about 20 DMET iterations to reach convergence. The total energy as well as AFM order converges at around the 10^{th} iteration, while the SC order oscillates until the 20^{th} iteration. This in part reflects the influence of the initial guess: the AFM guess [v^σ in Eq. (2)] is quite close to the converged potential, while the SC guess [$\Delta^{\alpha\beta}$ in Eq. (2)] is initialized randomly and thus needs more iterations to converge. If we were to restrict the DMET optimization to only pairing potentials with d-wave symmetry (as is commonly done in most cluster DMFT [85] or VCA calculations [37]), the convergence would be much faster. However, the more general form of the correlation potential in DMET allows for the possibility of other pairing channels and orders to emerge. The remaining DMET self-consistency error can be estimated from the difference between the expectation values (e.g. DMET energy) of the last two iterations [40], e.g. $\delta E = \frac{1}{2}|E(n-1) - E(n)|$. Consistent with our chosen convergence criterion, the typical size of the DMET self-consistency error in the undoped region is less than 10^{-5} (for both the energy and order parameters), and less than 10^{-4} (for the energy) and $\sim 10^{-3}$ (for the order parameters) in the doped region.

The error from the DMRG solver can be estimated using standard techniques based on the discarded weight in the DMRG calculation [69, 86, 87] and can be further reduced by extrapolation. The error in the impurity observables (used to evaluate the DMET energy and order parameters) is linear in the (sufficiently small) discarded weight δ and hence can be extrapolated to the exact result ($\delta = 0$) [87]. The convergence with bond dimension M for fixed correlation potential u is shown in Fig. 11. We find that the discarded weight in the normal state (undoped model) is extremely small and usually less than 10^{-8}, thus extrapolation is unnecessary. In fact, calculations can be carried out using a bond dimension as small as $M = 100$ without any significant error. On the other hand, when the system becomes superconducting, the discarded weight also increases, e.g. to 3×10^{-5} at $M = 800$, indicating that the system is more entangled. In such situations, extrapolation has a significant effect on the DMET expectation values. Compared to the extrapolated values, at $M = 800$ the error in the energy (per site) and order parameters is about 10^{-3}.

In summary, from the above analysis, we find that the DMET calculations can be smoothly converged, with minimal error

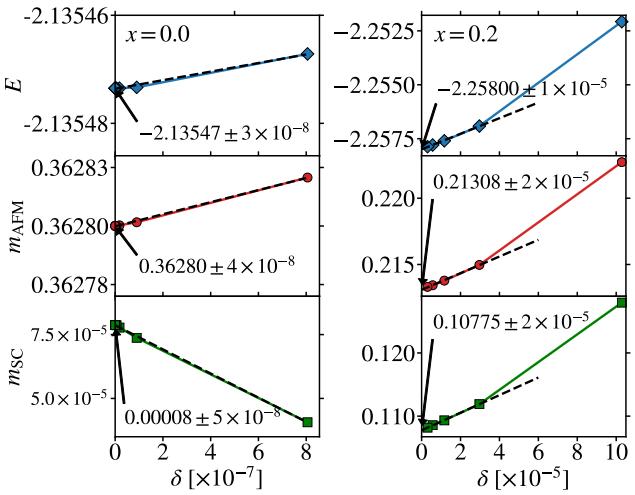

FIG. 11. DMET energy (in units of t_{pd}) and order parameters of the Hybertsen minimal parametrized three-band model, with respect to the discarded weight δ of the DMRG solver, at doping $x = 0.0$ (left) and $x = 0.2$ (right). The values are linearly extrapolated to the limit where $\delta = 0.0$ (dashed line). The error shown is the standard deviation of linear regression.

from either the self-consistency or from the solver.

[1] V. J. Emery, Theory of High-T_c Superconductivity in Oxides, Phys. Rev. Lett. **58**, 2794 (1987).

[2] J. Hubbard, Electron correlations in narrow energy bands, Proc. R. Soc. London A **276**, 238 (1963).

[3] P. W. Anderson, The Resonating Valence Bond State in La_2CuO_4 and Superconductivity, Science **235**, 1196 (1987).

[4] F. C. Zhang and T. M. Rice, Effective Hamiltonian for the superconducting Cu oxides, Phys. Rev. B **37**, 3759 (1988).

[5] H. Sakakibara, H. Usui, K. Kuroki, R. Arita, and H. Aoki, Two-Orbital Model Explains the Higher Transition Temperature of the Single-Layer Hg-Cuprate Superconductor Compared to That of the La-Cuprate Superconductor, Phys. Rev. Lett. **105**, 057003 (2010).

[6] J. LeBlanc, A. E. Antipov, F. Becca, I. W. Bulik, G. K.-L. Chan, C.-M. Chung, Y. Deng, M. Ferrero, T. M. Henderson, C. A. Jiménez-Hoyos, E. Kozik, X.-W. Liu, A. J. Millis, N. Prokof'ev, M. Qin, G. E. Scuseria, H. Shi, B. Svistunov, L. F. Tocchio, I. Tupitsyn, S. R. White, S. Zhang, B.-X. Zheng, Z. Zhu, and E. Gull, Solutions of the Two-Dimensional Hubbard Model: Benchmarks and Results from a Wide Range of Numerical Algorithms, Phys. Rev. X **5**, 041041 (2015).

[7] B.-X. Zheng, C.-M. Chung, P. Corboz, G. Ehlers, M.-P. Qin, R. M. Noack, H. Shi, S. R. White, S. Zhang, and G. K.-L. Chan, Stripe order in the underdoped region of the two-dimensional Hubbard model, Science **358**, 1155 (2017).

[8] B. Fauqué, Y. Sidis, V. Hinkov, S. Pailhès, C. T. Lin, X. Chaud, and P. Bourges, Magnetic Order in the Pseudogap Phase of High T_c Superconductors, Phys. Rev. Lett. **96**, 197001 (2006).

[9] M. S. Hybertsen, E. B. Stechel, M. Schluter, and D. R. Jennison, Renormalization from density-functional theory to strong-coupling models for electronic states in Cu-O materials, Phys. Rev. B **41**, 11068 (1990).

[10] R. T. Scalettar, D. J. Scalapino, R. L. Sugar, and S. R. White, Antiferromagnetic, charge-transfer, and pairing correlations in the three-band Hubbard model, Phys. Rev. B **44**, 770 (1991).

[11] M. Cini and A. Balzarotti, Cluster approach to the three-band Hubbard model of the Cu-O plane: Superconducting pairs, Phys. Rev. B **56**, 14711 (1997).

[12] M. Greiter and R. Thomale, No evidence for spontaneous orbital currents in numerical studies of three-band models for the cuo planes of high temperature superconductors, Phys. Rev. Lett. **99**, 027005 (2007).

[13] R. Thomale and M. Greiter, Numerical analysis of three-band models for cuo planes as candidates for a spontaneous t-violating orbital current phase, Phys. Rev. B **77**, 094511 (2008).

[14] T. Shirakawa, H. Watanabe, and S. Yunoki, Theoretical Studies of a Three-band Hubbard Model with a Strong Spin-orbit Coupling for 5d Transition Metal Oxide Sr_2IrO_4, J. Phys.: Conf. Ser. **454**, 012068 (2013).

[15] Y. Kung, C.-C. Chen, B. Moritz, S. Johnston, R. Thomale, and T. Devereaux, Numerical exploration of spontaneous broken symmetries in multiorbital hubbard models, Phys. Rev. B **90**, 224507 (2014).

[16] G. Dopf, A. Muramatsu, and W. Hanke, Three-band Hubbard model: A Monte Carlo study, Phys. Rev. B **41**, 9264 (1990).

[17] K. Kuroki and H. Aoki, Quantum Monte Carlo Evidence for Superconductivity in the Three-Band Hubbard Model in Two Dimensions, Phys. Rev. Lett. **76**, 4400 (1996).

[18] M. Guerrero, J. E. Gubernatis, and S. Zhang, Quantum Monte Carlo study of hole binding and pairing correlations in the three-band Hubbard model, Phys. Rev. B **57**, 11980 (1998).

[19] T. Yanagisawa, S. Koike, and K. Yamaji, Ground state of the three-band Hubbard model, Phys. Rev. B **64**, 184509 (2001).

[20] C. Weber, T. Giamarchi, and C. Varma, Phase diagram of a three-orbital model for high-t c cuprate superconductors, Phys. Rev. Lett. **112**, 117001 (2014).

[21] Y. F. Kung, C.-C. Chen, Y. Wang, E. W. Huang, E. A. Nowadnick, B. Moritz, R. T. Scalettar, S. Johnston, and T. P. Devereaux,

Characterizing the three-orbital Hubbard model with determinant quantum Monte Carlo, Phys. Rev. B **93**, 155166 (2016).
[22] E. W. Huang, C. B. Mendl, S. Liu, S. Johnston, H.-C. Jiang, B. Moritz, and T. P. Devereaux, Numerical evidence of fluctuating stripes in the normal state of high-T_c cuprate superconductors, Science **358**, 1161 (2017).
[23] E. Vitali, H. Shi, A. Chiciak, and S. Zhang, Metal-insulator transition in the ground state of the three-band hubbard model at half filling, Phys. Rev. B **99**, 165116 (2019).
[24] E. Jeckelmann, D. J. Scalapino, and S. R. White, Comparison of different ladder models, Phys. Rev. B **58**, 9492 (1998).
[25] S. Nishimoto, E. Jeckelmann, and D. J. Scalapino, Differences between hole and electron doping of a two-leg CuO ladder, Phys. Rev. B **66**, 245109 (2002).
[26] S. R. White and D. J. Scalapino, Doping Asymmetry and Striping in a Three-orbital CuO_2 Hubbard Model, Phys. Rev. B **92**, 205112 (2015).
[27] S. Bulut, W. A. Atkinson, and A. P. Kampf, Spatially modulated electronic nematicity in the three-band model of cuprate superconductors, Phys. Rev. B **88**, 155132 (2013).
[28] T. A. Maier and D. J. Scalapino, Pairing Interaction Near a Nematic Quantum Critical Point of a Three-band CuO_2 model, Phys. Rev. B **90**, 174510 (2014).
[29] W. A. Atkinson, A. P. Kampf, and S. Bulut, Charge order in the pseudogap phase of cuprate superconductors, New J. Phys. **17**, 013025 (2015).
[30] T. Maier, M. Zölfl, T. Pruschke, and J. Keller, Magnetic properties of the three-band Hubbard model, Eur. Phys. J. B **7**, 377 (1999).
[31] M. Zölfl, T. Maier, T. Pruschke, and J. Keller, Electronic properties of CuO_2-planes: A DMFT study, Eur. Phys. J. B **13**, 47 (2000).
[32] P. R. C. Kent, T. Saha-Dasgupta, O. Jepsen, O. K. Andersen, A. Macridin, T. A. Maier, M. Jarrell, and T. C. Schulthess, Combined density functional and dynamical cluster quantum Monte Carlo calculations of the three-band Hubbard model for hole-doped cuprate superconductors, Phys. Rev. B **78**, 035132 (2008).
[33] L. de' Medici, X. Wang, M. Capone, and A. J. Millis, Correlation Strength, Gaps, and Particle-hole Asymmetry in High-T_c Cuprates: A Dynamical Mean Field Study of the Three-band Copper-oxide Model, Phys. Rev. B **80**, 054501 (2009).
[34] C. Weber, C. Yee, K. Haule, and G. Kotliar, Scaling of the transition temperature of hole-doped cuprate superconductors with the charge-transfer energy, EPL **100**, 37001 (2012).
[35] A. Go and A. J. Millis, Spatial Correlations and the Insulating Phase of the High T_c Cuprates: Insights from a Configuration-Interaction-Based Solver for Dynamical Mean Field Theory, Phys. Rev. Lett. **114**, 016402 (2015).
[36] E. Arrigoni, M. Aichhorn, M. Daghofer, and W. Hanke, Phase Diagram and Single-particle Spectrum of CuO_2 high-T_c Layers: Variational Cluster Approach to the Three-band Hubbard Model, New J. Phys. **11**, 055066 (2009).
[37] W. Hanke, M. Kiesel, M. Aichhorn, S. Brehm, and E. Arrigoni, The 3-band Hubbard-model versus the 1-band model for the high-T_c cuprates: Pairing dynamics, superconductivity and the ground-state phase diagram, Eur. Phys. J. Spec. Top. **188**, 15 (2010).
[38] G. Knizia and G. K.-L. Chan, Density matrix embedding: A simple alternative to dynamical mean-field theory, Phys. Rev. Lett. **109**, 186404 (2012).
[39] I. W. Bulik, G. E. Scuseria, and J. Dukelsky, Density matrix embedding from broken symmetry lattice mean fields, Phys. Rev. B **89**, 035140 (2014).
[40] B.-X. Zheng and G. K.-L. Chan, Ground-state phase diagram of the square lattice Hubbard model from density matrix embedding theory, Phys. Rev. B **93**, 035126 (2016).
[41] B.-X. Zheng, J. S. Kretchmer, H. Shi, S. Zhang, and G. K.-L. Chan, Cluster size convergence of the density matrix embedding theory and its dynamical cluster formulation: A study with an auxiliary-field quantum Monte Carlo solver, Phys. Rev. B **95**, 045103 (2017).
[42] X. Wu, Z.-H. Cui, Y. Tong, M. Lindsey, G. K.-L. Chan, and L. Lin, Projected density matrix embedding theory with applications to the two-dimensional hubbard model, J. Chem. Phys. **151**, 064108 (2019).
[43] G. Knizia and G. K.-L. Chan, Density Matrix Embedding: A Strong-Coupling Quantum Embedding Theory, J. Chem. Theory Comput. **9**, 1428 (2013).
[44] S. Wouters, C. A. Jiménez-Hoyos, Q. Sun, and G. K.-L. Chan, A Practical Guide to Density Matrix Embedding Theory in Quantum Chemistry, J. Chem. Theory Comput. **12**, 2706 (2016).
[45] H. Q. Pham, V. Bernales, and L. Gagliardi, Can Density Matrix Embedding Theory with the Complete Activate Space Self-Consistent Field Solver Describe Single and Double Bond Breaking in Molecular Systems?, J. Chem. Theory Comput. **14**, 1960 (2018).
[46] I. W. Bulik, W. Chen, and G. E. Scuseria, Electron correlation in solids via density embedding theory, J. Chem. Phys. **141**, 054113 (2014).
[47] Z.-H. Cui, T. Zhu, and G. K.-L. Chan, Efficient implementation of ab initio quantum embedding in periodic systems: Density matrix embedding theory, J. Chem. Theory Comput. **16**, 119 (2020).
[48] H. Q. Pham, M. R. Hermes, and L. Gagliardi, Periodic electronic structure calculations with density matrix embedding theory, J. Chem. Theory Comput. **16**, 130 (2020).
[49] Z. Fan and Q.-l. Jie, Cluster density matrix embedding theory for quantum spin systems, Phys. Rev. B **91**, 195118 (2015).
[50] B. Sandhoefer and G. K.-L. Chan, Density matrix embedding theory for interacting electron-phonon systems, Phys. Rev. B **94**, 085115 (2016).
[51] G. H. Booth and G. K.-L. Chan, Spectral functions of strongly correlated extended systems via an exact quantum embedding, Phys. Rev. B **91**, 155107 (2015).
[52] C. Sun, U. Ray, Z.-H. Cui, M. Stoudenmire, M. Ferrero, and G. K.-L. Chan, Finite-temperature density matrix embedding theory, Phys. Rev. B **101**, 075131 (2020).
[53] J. S. Kretchmer and G. K.-L. Chan, A real-time extension of density matrix embedding theory for non-equilibrium electron dynamics, J. Chem. Phys. **148**, 054108 (2018).
[54] M. S. Hybertsen, M. Schlüter, and N. E. Christensen, Calculation of Coulomb-interaction Parameters for La_2CuO_4 using a Constrained-density Functional Approach, Phys. Rev. B **39**, 9028 (1989).
[55] A. K. McMahan, J. F. Annett, and R. M. Martin, Cuprate parameters from numerical Wannier functions, Phys. Rev. B **42**, 6268 (1990).
[56] R. L. Martin, Electronic localization in the cuprates, Phys. Rev. B **53**, 15501 (1996).
[57] M. Hirayama, Y. Yamaji, T. Misawa, and M. Imada, Ab initio effective Hamiltonians for cuprate superconductors, Phys. Rev. B **98**, 134501 (2018).
[58] A. Chiciak, E. Vitali, H. Shi, and S. Zhang, Magnetic orders in the hole-doped three-band Hubbard model: Spin spirals, nematicity, and ferromagnetic domain walls, Phys. Rev. B **97**, 235127 (2018).
[59] I. Peschel, Special Review: Entanglement in Solvable Many-

Particle Models, Braz. J. Phys. **42**, 267 (2012).
[60] P.-G. de Gennes, Superconductivity of Metals and Alloys (Benjamin, New York, 1966).
[61] B.-X. Zheng, Density Matrix Embedding Theory and Strongly Correlated Lattice Systems, arXiv: 1803.10259 [cond-mat] (2018).
[62] B.-X. Zheng, https://bitbucket.org/zhengbx/libdmet.
[63] Z.-H. Cui, https://github.com/zhcui/libdmet_solid.
[64] S. R. White, Density matrix formulation for quantum renormalization groups, Phys. Rev. Lett. **69**, 2863 (1992).
[65] S. R. White, Density-matrix algorithms for quantum renormalization groups, Phys. Rev. B **48**, 10345 (1993).
[66] Q. Sun, T. C. Berkelbach, N. S. Blunt, G. H. Booth, S. Guo, Z. Li, J. Liu, J. D. McClain, E. R. Sayfutyarova, S. Sharma, S. Wouters, and G. K.-L. Chan, PySCF: the Python-based simulations of chemistry framework, WIREs Comput. Mol. Sci. **8**, e1340 (2018).
[67] Q. Sun, X. Zhang, S. Banerjee, P. Bao, M. Barbry, N. S. Blunt, N. A. Bogdanov, G. H. Booth, J. Chen, Z.-H. Cui, J. J. Eriksen, Y. Gao, S. Guo, J. Hermann, M. R. Hermes, K. Koh, P. Koval, S. Lehtola, Z. Li, J. Liu, N. Mardirossian, J. D. McClain, M. Motta, B. Mussard, H. Q. Pham, A. Pulkin, W. Purwanto, P. J. Robinson, E. Ronca, E. Sayfutyarova, M. Scheurer, H. F. Schurkus, J. E. T. Smith, C. Sun, S.-N. Sun, S. Upadhyay, L. K. Wagner, X. Wang, A. White, J. D. Whitfield, M. J. Williamson, S. Wouters, J. Yang, J. M. Yu, T. Zhu, T. C. Berkelbach, S. Sharma, A. Sokolov, and G. K.-L. Chan, Recent developments in the pyscf program package, J. Chem. Phys. **153**, 024109 (2020).
[68] C. Edmiston and K. Ruedenberg, Localized Atomic and Molecular Orbitals, Rev. Mod. Phys. **35**, 457 (1963).
[69] G. K.-L. Chan and M. Head-Gordon, Highly correlated calculations with a polynomial cost algorithm: A study of the density matrix renormalization group, J. Chem. Phys. **116**, 4462 (2002).
[70] G. K.-L. Chan, An algorithm for large scale density matrix renormalization group calculations, J. Chem. Phys. **120**, 3172 (2004).
[71] G. K.-L. Chan and S. Sharma, The Density Matrix Renormalization Group in Quantum Chemistry, Annu. Rev. Phys. Chem. **62**, 465 (2011).
[72] S. Sharma and G. K.-L. Chan, Spin-adapted density matrix renormalization group algorithms for quantum chemistry, J. Chem. Phys. **136**, 124121 (2012).
[73] P. Pulay, Convergence Acceleration of Iterative Sequences. The Case of SCF Iteration, Chem. Phys. Lett. **73**, 393 (1980).
[74] P. Pulay, Improved SCF convergence acceleration, J. Comput. Chem. **3**, 556 (1982).
[75] K. Yamada, E. Kudo, Y. Endoh, Y. Hidaka, M. Oda, M. Suzuki, and T. Murakami, The Effect of the Heat Treatments on the Antiferromagnetism in $La_2CuO_{4-\delta}$ Single Crystals, Solid State Commun. **64**, 753 (1987).
[76] Y. Tokura, S. Koshihara, T. Arima, H. Takagi, S. Ishibashi, T. Ido, and S. Uchida, Cu-O Network Dependence of Optical Charge-transfer Gaps and Spin-pair Excitations in Single-CuO_2-layer Compounds, Phys. Rev. B **41**, 11657 (1990).
[77] S. L. Cooper, G. Thomas, A. Millis, P. Sulewski, J. Orenstein, D. Rapkine, S.-W. Cheong, and P. Trevor, Optical studies of gap, exchange, and hopping energies in the insulating cuprates, Phys. Rev. B **42**, 10785 (1990).
[78] S. Uchida, T. Ido, H. Takagi, T. Arima, Y. Tokura, and S. Tajima, Optical Spectra of $La_{2-x}Sr_xCuO_4$: Effect of Carrier Doping on the Electronic Structure of the CuO_2 Plane, Phys. Rev. B **43**, 7942 (1991).
[79] H. Romberg, N. Nücker, J. Fink, T. Wolf, X. Xi, B. Koch, H. Geserich, M. Dürrler, W. Assmus, and B. Gegenheimer, Dielectric function of $YBa_2Cu_3O_7$ between 50 mev and 50 ev, Z. Phys., B, Condens. matter. **78**, 367 (1990).
[80] See Supplemental Material at http://link.aps.org/supplemental/10.1103/PhysRevResearch.2.043259 for the AFM order of the one-band Hubbard model, AFM and SC order of Hybertsen and Martin models, additional figures of charge, spin and pairing patterns of the three-band model and the derivation of the analytic gradient of the cost function.
[81] J. Jefferson, H. Eskes, and L. Feiner, Derivation of a single-band model for CuO_2 planes by a cell-perturbation method, Phys. Rev. B **45**, 7959 (1992).
[82] A. Damascelli, Z. Hussain, and Z.-X. Shen, Angle-resolved photoemission studies of the cuprate superconductors, Rev. Mod. Phys. **75**, 473 (2003).
[83] T. Timusk and B. Statt, The pseudogap in high-temperature superconductors: An experimental survey, Rep. Prog. Phys. **62**, 61 (1999).
[84] P. A. Lee, N. Nagaosa, and X.-G. Wen, Doping a Mott Insulator: Physics of High-Temperature Superconductivity, Rev. Mod. Phys. **78**, 17 (2006).
[85] D. Sénéchal, An introduction to quantum cluster methods, arXiv: 0806.2690 [cond-mat] (2008).
[86] Ö. Legeza and G. Fáth, Accuracy of the density-matrix renormalization-group method, Phys. Rev. B **53**, 14349 (1996).
[87] S. R. White and A. L. Chernyshev, Néel Order in Square and Triangular Lattice Heisenberg Models, Phys. Rev. Lett. **99**, 127004 (2007).